Landslides
DOI 10.1007/s10346-020-01533-0
Received: 11 January 2020
Accepted: 10 September 2020

Yuankun Xu · David L. George · Jinwoo Kim · Zhong Lu · Mark Riley · Todd Griffin · Juan de la Fuente

Landslide monitoring and runout hazard assessment by integrating multi-source remote sensing and numerical models: an application to the Gold Basin landslide complex, northern Washington

Abstract The landslide complex at Gold Basin, Washington, has been drawing considerable attention after a catastrophic runout of the nearby landslide at Oso, Washington, in 2014. To evaluate potential threats of the Gold Basin landslide to the campground down the slope, remote sensing and numerical modeling were integrated to monitor recent landslide activity and simulate hypothetical runout scenarios. Bare-earth LiDAR DEM (digital elevation model) differencing, InSAR (Interferometric Synthetic Aperture Radar), and offset tracking of SAR images reveal that localized collapses at the headscarps have been the primary type of landslide activity at Gold Basin from 2005 to 2019, and currently no signs indicative of movement of a large centralized block or a deep-seated main body were detected. The maximum horizontal deformation rate is 5 m/year occurring primarily from headscarp recession of the middle lobe, and the annual landsliding volume of the whole landslide complex averages 1.03×10^5 m^3. From three-dimensional limit equilibrium analysis of generalized terrace structures, the maximum landslide volume is estimated as 2.0×10^6 m^3. Simulations of hypothetical runout scenarios were carried out using the depth-averaged two-phase model D-claw with above-obtained landslide geometry constraints. The simulation results demonstrate that debris flows with volume less than 10^5 m^3 only pose limited threats to the campground, while volumes over 10^6 m^3 could cause severe damages. Consequently, the estimated maximum landslide volume of 2.0×10^6 m^3 suggests a potential risk to the campground nearby. Adaption of our methodology could prove useful for evaluating other similar landslides globally for hazards prevention and mitigation.

Keywords Slope stability · Remote sensing · SAR · Debris flow · Runout modelling

Introduction

The Gold Basin landslide in Washington has been drawing considerable attention from officials and local residents after the devastating 2014 landslide at Oso, Washington (Wartman et al. 2016; Iverson et al. 2015), which damaged 49 houses down the slope and caused 43 fatalities. The two landslides are separated by only 23 km (Fig. 1a) and have measurable similarities in terms of terrain setting, slope angle, and historical failures. Both slides have rivers flowing through the toes that influence landslide processes by eroding the landslide toe, and could potentially increase flow mobility and inundation extent in the event of a failure. An important distinction between these two landslides is their morphological settings. The landslide complex at Gold Basin is comprised of three separate stream valleys with deeply incised channels (Fig. 1b). The valleys contain deep-seated landslide deposits which form moderately sized landslide blocks with gentle, hummocky terrain immediately upslope from the channel incisions (Fig. 1b, d). In contrast, the landslide at Oso, WA expresses a distinct stairstep pattern typical of a recent landslide involving large blocks (Fig. 1c, e, f). Comparison of the hillshade images of Gold Basin and Oso suggests that the landslide complex at Gold Basin may have experienced a large event similar in size to the 2014 event at Oso (Figs. 1c and 2a), but the original landforms have been greatly modified by subsequent fluvial erosion and mass wasting (Fig. 2a).

For the Gold Basin landslide, runout events pose direct threats to a popular campground located on the opposite side of the Stillaguamish River (Fig. 2a). The campground has been closed since 2014 out of safety concerns, and a detailed hazard assessment is required prior to reopening. In addition to a potential runout event, fine-grained sediments derived from the landslide complex have been persistently transported into the South Fork Stillaguamish River where it negatively impacts migrant salmon spawning grounds that are of critical importance to the Stillaguamish Tribe (Shannon Wilson Engineers 1954; Staisch 2018). To better evaluate the Gold Basin landslide complex, we utilized both remote sensing and numerical simulations to assess slope stability and evaluate the potential inundation extent.

Field surveys are traditionally relied upon for monitoring landslide movement and slope stability. Ground instrumentation, such as GPS, extensometers, and tiltmeters, provides reliable and accurate measurements and has been widely used for monitoring dangerous landslides that directly threaten human safety (Angeli et al. 2000; Terzis et al. 2006). In addition, remote sensing techniques that exploit increasingly available data resources such as LiDAR (Light Detection and Ranging) DEMs, space- and airborne optical images, and SAR (Synthetic Aperture Radar), which provide remote access with wide spatial, radiometric, spectral, and temporal coverage, have greatly improved the efficiency of landslide detection and mapping (e.g., Fruneau et al. 1996; Squarzoni et al. 2003; Colesanti and Wasowski 2006; Xu et al. 2019). However, despite multiple available data sources, remote sensing surveillance of slopes in particular terrains and at certain times still presents challenges due to current technical limitations. The effectiveness of utilizing SAR images for landslide studies depends on their spatial resolution, wavelength of the SAR signal, the revisit cycle of SAR satellites, the look angle of SAR sensors, and the motion rate of landslides (e.g., the InSAR method may not be effective for rapidly moving slides), while that of LiDAR is primarily affected by available repeated acquisitions. For the free or low-cost optical images from satellite platforms such as Landsat and Sentinel-2, coarse spatial resolution and cloud coverage are the

Published online: 07 October 2020

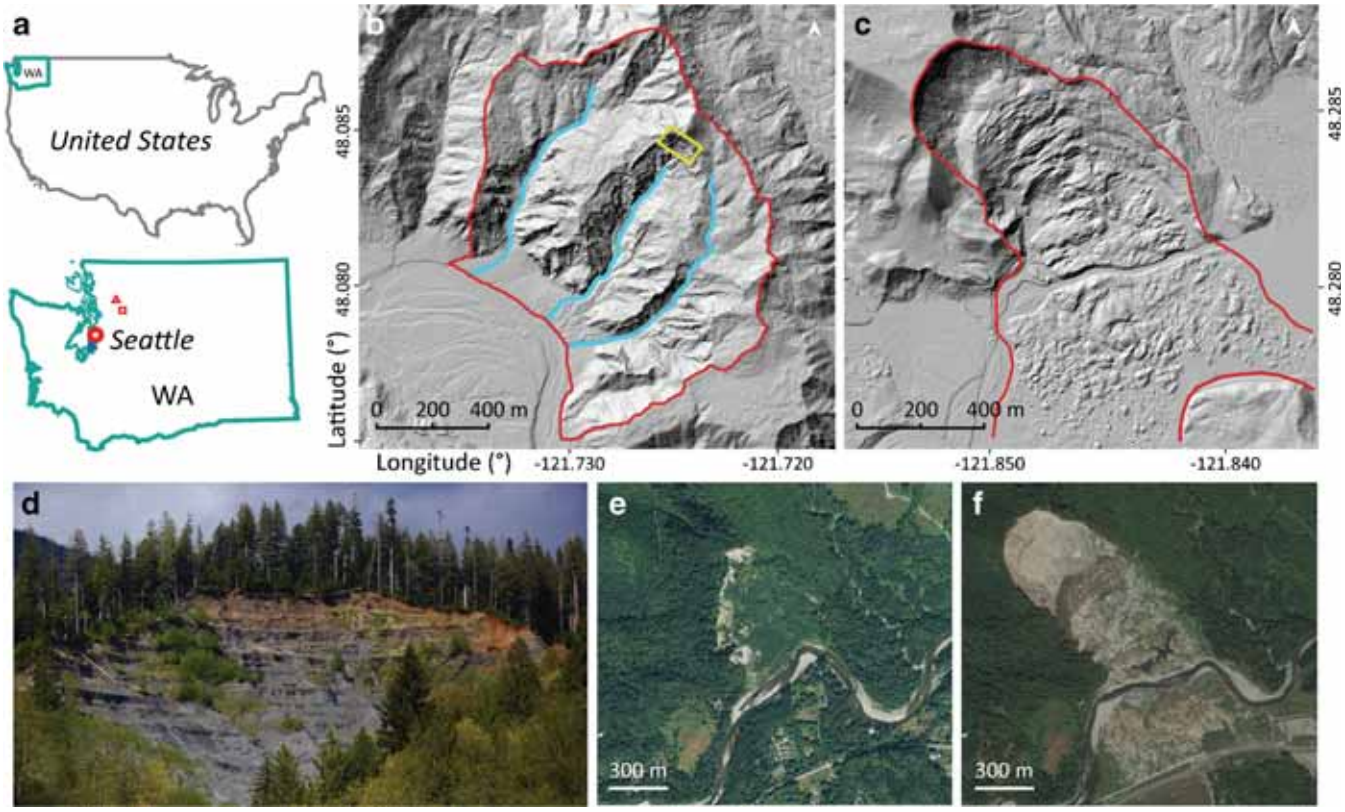

Fig. 1 Comparison between the Gold Basin landslide and the Oso landslide. **a** Geographic locations of the Gold Basin landslide complex (red square) and the Oso landslide (red triangle), with the annotation WA=Washington. Hillshade images of **b** Gold Basin landslide complex (red polygon) and **c** Oso landslide. Cyan polylines in **b** represent stream valleys and the yellow square outlines the headscarp shown in **d**. True-color images of Oso slide **e** before and **f** after the 2014 runout event. Images were obtained from Google Earth. LiDAR DEMs were accessed from the Washington State Department of Natural Resources

two key limiting factors. Consequently, a single remote sensing device might not be adequate to detect and monitor some landslide scenarios (e.g., a small localized collapse of a steep slope at a particular time). Nevertheless, integrating multiple remotely sensed datasets and employing suitable interpretation methods provide a potential solution for certain difficult cases.

In order to evaluate the potential runout and inundation extent, should a slope failure lead to a rapidly flowing landslide and debris flow, we employed numerical modeling using the D-claw package (George and Iverson 2014). D-claw is a depth-averaged two-phase model that simulates granular flow dynamics based on conservation of mass and momentum, and accounting for the important feedbacks between solid grain concentrations and the basal pore-fluid pressure that regulate flow resistance and mobility, based in part on the theory of granular dilatancy for shearing soils (Iverson and George 2014). Running a D-claw model requires a hypothetical landslide basal slip surface that defines the initial landslide volume and geometry (George and Iverson 2014; Iverson et al. 2015).

This investigation focuses on using multiple remote sensing datasets to monitor movement of the Gold Basin landslide complex, which also helps constrain initial, hypothetical landslide source geometries as an input for the D-claw simulations of runout scenarios. Due to the steep slopes and large yet localized deformation, multiple SAR processing methods are employed to characterize the landslide motions. D-claw simulations are subsequently performed to evaluate the potential hazard zone. Our methodology of evaluating landslide runout hazards developed for this case study can be easily adapted for other similar landslides globally to assist on hazard prevention and mitigation.

Geological setting and history

Regional setting

The Gold Basin landslide complex, located in Snohomish County, Washington (Fig. 1a, b), lies above the South Fork of the Stillaguamish River in the Cascade Range (Fig. 2a). The landslide complex's elevation ranges from 325 to 495 m above sea level and consists of three small, steep tributary valleys that form three separate lobes on the north valley wall and transport landslide debris and sediment downstream to the Stillaguamish River through valley channels (Fig. 1b). The valleys at Gold Basin were originally filled with recessional glacial deposits to a substantial depth of 175 m. The river has cut through deposits (Benda and Collins 1992; Staisch 2018) and form steep-sided valley walls exposing the glacial stratigraphy (Miller and Miller 1999; Miller 2019). Stratigraphy is vertically and laterally heterogeneous with discontinuous lenses of silt and clay interspersed in sandy river deposits. Field observations and lab tests indicate that there is a 52.6-m-thick water-perching layer (400.9–453.5 m above sea level) of silt and clay between strata of poorly sorted gravels and sands in the stratigraphy of the middle lobe (Fig. 2b; McCabe 2016).

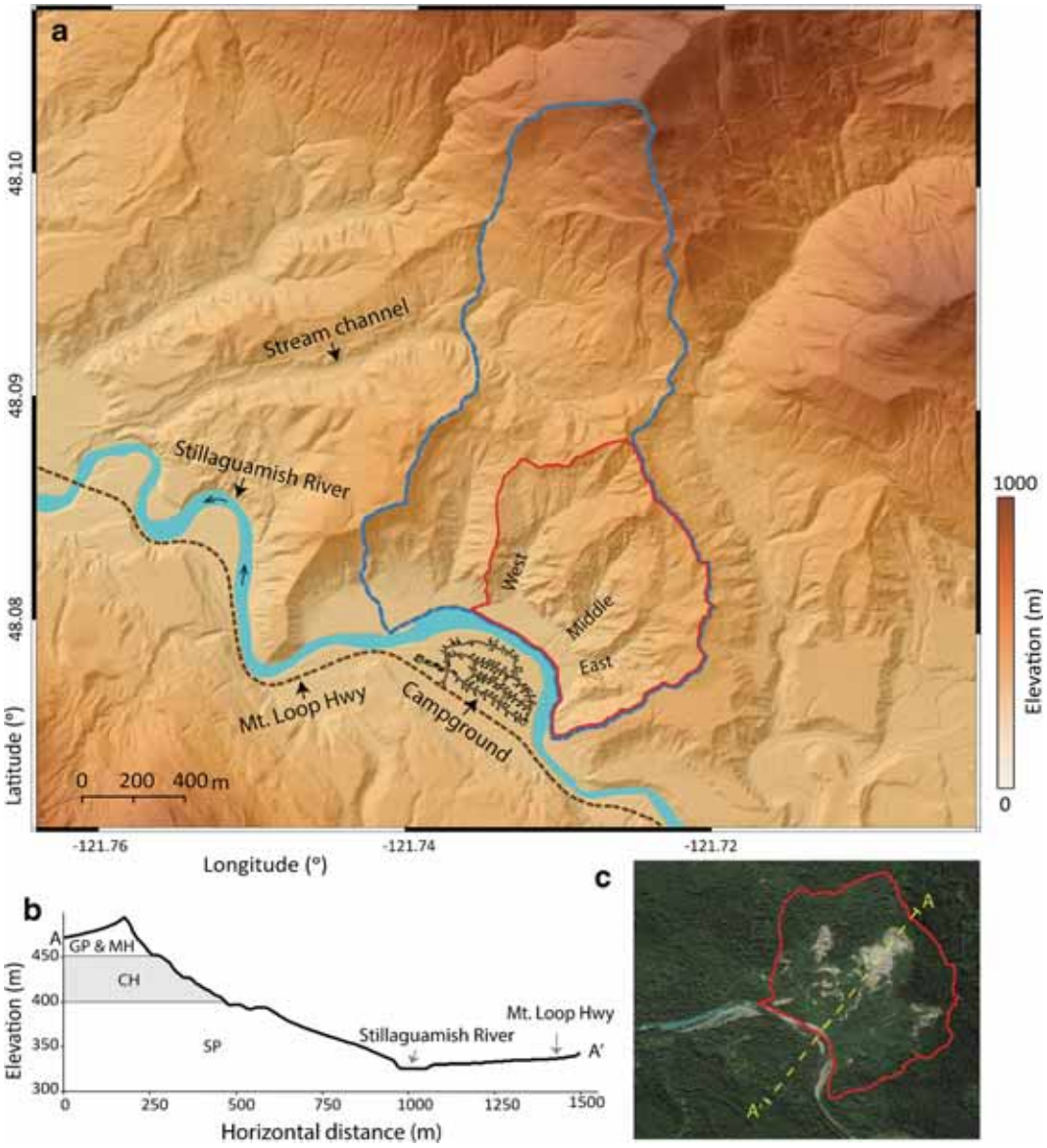

Fig. 2 Geographical and geological setting of the Gold Basin landslide complex. **a** The Gold Basin landslide (red polygon) comprises part of a larger landslide complex (dashed blue polygon) that is bisected by a stream channel (annotated as Stream channel in Fig. 2a). A campground is located on the opposite side of the South Fork Stillaguamish River. **b** Elevation profile along A-A′ in **c** and a generalized stratigraphy obtained by McCabe (2016). Soil types were classified following the Unified Soil Classification System (USCS), with GP=poorly graded gravel, MH=silt of high plasticity and elastic silt, CH=clay of high plasticity and fat clay, and SP=poorly graded sand. **c** A true-color image of the slide obtained in July 2018 from Google Earth

Historical landslide activity

Three relatively large historical runout events have been recorded at Gold Basin, though the involved lobes varied over time. Cycles of small localized collapses and erosion have been occurring intermittently over many decades, followed by subsequent revegetation. The earliest recoded landslide activity can be traced back to 1942 (Benda and Collins 1992). The landslide source was confined to the lower portions of the middle lobe and the eastern-most lobe, and the active area was approximately a quarter of the much larger 1964 landslide. The 1964 event occurred in the eastern-most lobe and formed a fan at the mouth of that lobe, as indicated by the exposed bare ground in aerial images (Fig. 3; Miller and Miller 1999). Subsequent vegetation regrowth eventually obscured the fan, and by 1983 the river had eroded back the toe of the eastern-most lobe (Miller 2019). The most recent debris flow occurred in 1996, in the middle and western-most lobes. Debris deposits blocked the river and had shifted the channel to the south where it currently remains. The evolution of the channel course is apparent by comparing the 1995 and 2007 images of the site (Fig. 3).

Methodology and data

Measuring landslide movement using remote sensing

LiDAR DEM differencing

LiDAR DEMs have proven to be an effective tool for landslide detection because of their high spatial resolution and high

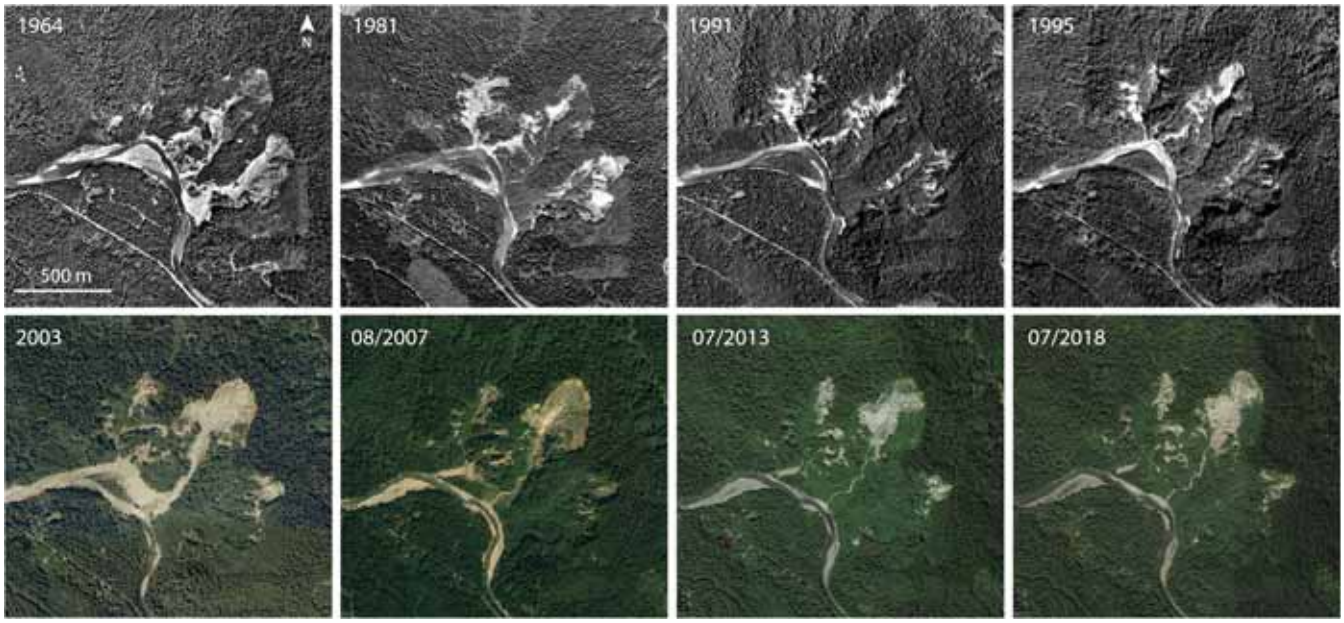

Fig. 3 Historical images of the Gold Basin landslide. The 1964–2003 figures are adapted from Miller and Miller (1999) and Miller (2019). Bright features represent areas with bare ground. The 2007–2018 figures were obtained from Google Earth

measurement accuracy (e.g., Hodgson et al. 2003; Roering et al. 2009). The sub-meter-level spatial resolution and the centimeter-level absolute accuracy provide reliable and accurate measurements of landslide motions, ranging from localized small displacements to large runout events. Moreover, landslide detection with LiDAR point clouds is largely impervious to the influence of vegetation, slope angle, and ground features. However, at the state level, there is presently limited LiDAR spatial coverage, and typically the datasets are very sparse in terms of repeated temporal sampling. Considering the Gold Basin region, for example, LiDAR DEMs are only available for years 2005, 2006, 2013, and 2016 and lack full spatial continuity for the project area, which is essential for differencing. Nevertheless, hillshade images produced from high-resolution DEMs facilitate interpretation of landforms and provide insights into the landslide processes (Fig. 2a). In this investigation, we applied DEM differencing to all available LiDAR DEMs in the Gold Basin region to quantify the deformation rates and landslide volumes from 2005 to 2016.

InSAR

InSAR (Interferometric Synthetic Aperture Radar) methods are focused on the phase information of SAR backscattering and can optimally provide up to millimeter-level measurement accuracy along the LOS (line of sight) direction (e.g., Hanssen 2001). However, substantial pixel displacements can present coherence degradation and unwrapping problems (e.g., Lu and Dzurisin 2014). Consequently, applying InSAR to measure landslide movements with high deformation gradients (phase difference between two adjacent pixels exceeds $\pi/2$) requires additional data inputs or assumptions of displacement patterns (e.g., Xu et al. 2019). The long-wavelength L-band data generally maintain better coherence in vegetated terrains and yield better interferometric results than the shorter wavelength C-band and X-band SAR images (Xu et al. 2019).

As LiDAR DEMs are unavailable after 2016, we processed all available SAR data from the L-band ALOS-2 PALSAR-2, the C-band Sentinel-1A/B, and the X-band TerraSAR-X to detect recent landslide activities between 2017 and 2019 using the InSAR method.

SAR intensity differencing and pixel offset tracking

SAR intensity refers to the strength of the reflected signal from ground objects. Landslide activity that causes measurable changes of the backscattering signal can be detected by differencing SAR intensity images (e.g., Plank et al. 2016). However, solely differencing SAR intensity changes cannot confirm a landslide activity, as other factors, such as changes in soil moisture and variations in forest-cover density (associated with wildfire, disease, or silvicultural activities such as timber harvest thinning or fuel management), also cause fluctuation of backscattering signals. An alternate approach is to track pixel offsets between two SAR intensity images using cross correlation (e.g., Strozzi et al. 2002; Singleton et al. 2014). The offset tracking accuracy can reach 1/20 to 1/10 pixels (Hanssen 2001). We applied both SAR intensity differencing and pixel offset tracking to detect recent landslide activity at Gold Basin.

First, we implemented intensity change detection methods on the high-spatial-resolution TerraSAR-X data from Jan 2017 to March 2019 to detect the existence of highly localized deformations. As a single-look SAR image generally contains significant speckle noises (e.g., Hanssen 2001), we multi-looked every image with a 3×3 multi-look factor and averaged five images acquired in the same season to form one image for detecting intensity changes. Three SAR intensity images of years 2017, 2018, and 2019 were generated by averaging SAR images acquired between January and

March in corresponding years (~ 5 images for each year), and then utilized to calculate intensity changes.

Second, we applied the pixel offset tracking method to the same Tandem-X datasets from 2017 to 2019. Unlike the intensity change detection, pixel offset tracking can provide quantitative measurements of landslide movement. Similarly, we averaged five SAR intensity images between January and March of each year, before conducting offset tracking. Here, we did not employ multi-looking, because multi-looking would increase pixel size and consequently reduce offset tracking accuracy. Pixel offset tracking was carried out twice iteratively with downscaling window sizes. A window size of 64 × 64 pixels was set for the first round of offset tracking, and the output was used as the input for the second round of offset tracking after eliminating offset anomalies. The second round started with a smaller window size of 32 × 32 pixels, and the final results were smoothed using a moving window of 2 × 2 pixels.

Runout scenario simulation

D-claw model

D-claw is a depth-averaged two-phase model that combines the concepts of critical-state soil mechanics, grain-flow mechanics, and fluid dynamics (Iverson and George 2014). The model's five balance equations describe coupled evolution of the solid volume fraction, basal pore-fluid pressure, flow thickness, and two components of flow velocity. The model incorporates the theory of soil dilatancy in order to mediate the feedback effects of soil-shearing and fluid-pressure-dependent mobility and resistance (Iverson and George 2014). Adjustable parameters in the model are based on well-established and measurable material quantities (e.g., initial porosity, hydraulic permeability, solid-matrix elastic compressibility) In lieu of site-specific studies of these parameters, they are constrained to reasonable bounds by sediment tests of materials in analogous studies or geologically similar regions (see, e.g., Iverson et al. 2010, 2015).

The predicted debris flow behavior initiated from a landslide failure is influenced by several non-dimensional quantities identified by Iverson and George (2014) and depends on landslide initial conditions and evolving material properties. These quantities include the difference between the initial solid volume fraction of sediment and an evolving equilibrium solid volume fraction, $m_o - m_{eqm}$. The evolving equilibrium volume fraction m_{eqm} depends on the state of flow variables and an initial, or critical equilibrium m_{crit}, which represents the quasi-static equilibrium volume fraction prior to motion. The sign of $m_o - m_{eqm}$ determines whether soils are in a contractive state in which initial shearing leads to increased mobility, or a dilative state in which shearing decreases mobility. The two alternative states of the material lead to either positive feedbacks and flow acceleration or negative feedbacks and flow stabilization and deposition. For characterizing hazards that may result from high-mobility landslides, the former, generally a contractive initial state of debris is assumed.

Log-spiral basal surfaces

To simulate hypothetical runout scenarios using the D-claw package, landslide basal slip surfaces are required. In lieu of additional site-specific data, basal surfaces are typically assumed to have longitudinal transects that conform to a logarithmic-spiral shape, a commonly assumed feature of idealized landslide scarps. For a homogeneous slope and assuming a visco-elastic rheology of shearing soils, the Mohr-Coulomb yield criterion leads to a logarithmic-spiral failure surface (Baker and Garber 1978; Chen 1975). In a polar coordinate system, the log-spiral is described as

$$r = r_o e^{\theta \tan\phi} \quad (1)$$

where r is the spiral radius, θ is the rotation angle with clockwise from the horizontal being positive, r_o is the radius value for θ=0°, and ϕ is the internal friction angle of landslide material.

In the longitudinal direction, a vertical profile of the basal surface can be uniquely determined if two intersection points with the ground topography and the two corresponding intersection angles are given. A continuous three-dimensional basal surface can be constructed by interpolating or fitting multiple longitudinal log-spiral profiles. For smoother surfaces, fitting multiple curves in the transverse direction can be employed. We used the 2016 bare-earth LiDAR DEM for constructing hypothetical log-spiral basal surfaces and for runout topography.

Landslide volume estimations

We obtained the annual average movement volume of the Gold Basin landslide complex as 1.03×10^5 m^3/year by differencing the 2005 and 2016 LiDAR DEMs.

The maximum landslide volume was estimated from the soil stratigraphy of the Gold Basin landslide complex (Fig. 2b) based on Perkins et al.'s (2017) simplified model. Three-dimensional limit equilibrium analysis of typical glacial stratigraphy consisting of a weak unit (advance glaciolacustrine deposits) between two strong units (advance outwash sands) in northern Washington demonstrates that the thickness and position of the weak unit exert a considerable influence on potential landslide volumes (Perkins et al. 2017). In fact, typical landslide volumes can be readily estimated based on geographical information regarding the geometry of the weak layer and the location of the landslide. Such estimates have been performed and validated by field surveys of multiple landslides along the Skagit River and North Fork Stillaguamish River regions (Perkins et al. 2017). For instance, the estimated maximum volume for the Oso landslide is 9.8×10^6 m^3 (Fig. 4), close to the volume of 7.3×10^6 to 9.2×10^6 m^3 measured from LiDAR DEMs (Iverson et al. 2015). For the Gold Basin landslide, terrace height above the Stillaguamish River is 170 m; thickness of the weak layer composed of clays and silts is 52.6 m; and the elevation difference between the layer top and Stillaguamish River is 128.5 m (Fig. 2b). Applying Perkins et al.'s (2017) simplified model (Fig. 4) in this case implies an estimate of 2.0×10^6 m^3 for the maximum landslide volume.

D-claw simulation setup

To evaluate potential inundation extents of the Gold Basin landslide complex, we simulated 12 scenarios. These scenarios can be categorized into two groups, with each group employing a single value of $m_o - m_{crit}$. Six different initial volumes ranging from 5.7×10^4 to 4.5×10^6 m^3 were simulated for each group. We set m_{crit}=0.62 in all of the scenarios, which is commensurate with material that has a relatively high mud content of the formed debris (McCabe 2016; Iverson et al. 2010). Values satisfying $m_o < m_{crit}$ correspond to relatively mobile debris flows that are

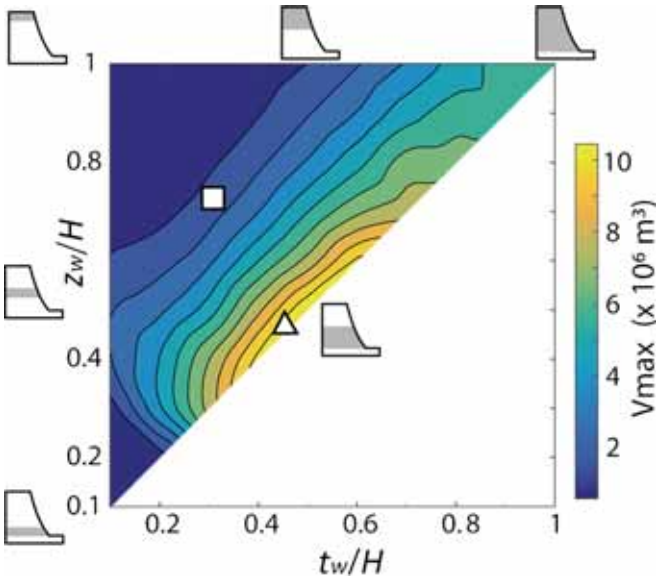

Fig. 4 Estimated maximum landslide volume within 10% of minimum FoS (factor of safety). The figure was adapted from Perkins et al. (2017). Square and triangle denote Gold Basin landslide (2.0×10^6 m^3) and Oso landslide (9.8×10^6 m^3) respectively. Z_w and t_w stand for bed-top height and thickness of the weak layer respectively, and H denotes thickness of the whole terrace

contractive, which is believed to be representative of the 2014 debris flow that occurred at Oso, Washington (Iverson et al. 2015), while $m_o > m_{crit}$ corresponds to less mobile runout behaviors as soils dilate during failure (Iverson et al. 2000).

Results

Remote sensing of landslide activity

LiDAR DEM differencing

Differencing of 2005 and 2016 DEMs reveals that substantial localized deformation of the western-most and middle lobes occurred, with a maximum displacement of ~ 30 m, while only slight deformation was observed at the eastern-most lobe (Fig. 5a). From 2013 to 2016, some localized yet substantial collapses (about 10 m in displacement) appeared at the headscarp of the middle lobe (Fig. 5b). Similar substantial deformation was also captured by terrestrial LiDAR from July 2015 to January 2016 (McCabe 2016). As the overlap region of the 2013 and 2016 DEMs only covers the head section of the slope, it is not clear whether localized movements also occurred at the lower sections from 2013 to 2016. Nearly no deformation occurred between June 2005 and March 2006.

InSAR

We processed all available SAR acquisitions from ALOS-2 PALSAR-2, Sentinel-1A/B, and TerraSAR-X. However, only the L-band ALOS-2 imagery produced useful interferograms for identifying ground deformation due to severe coherence loss of the shorter-wavelength C-band Sentinel-1A/B and X-band TerraSAR-X images. Five active landslides nearby Gold Basin were detected

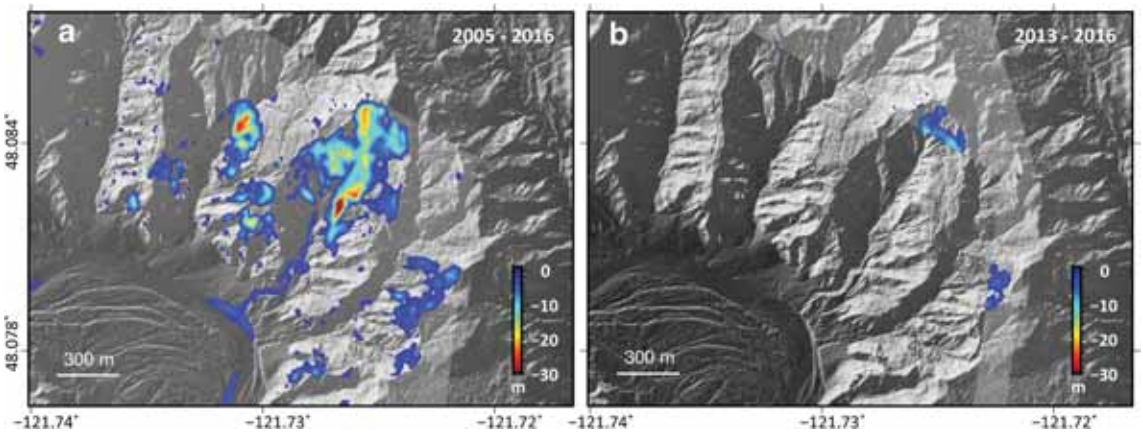

Fig. 5 Slope deformation captured by LiDAR DEMs. DEM changes **a** from 2005 to 2016 and **b** from 2013 to 2016. Slightly white-shaded regions represent overlaps of two DEMs

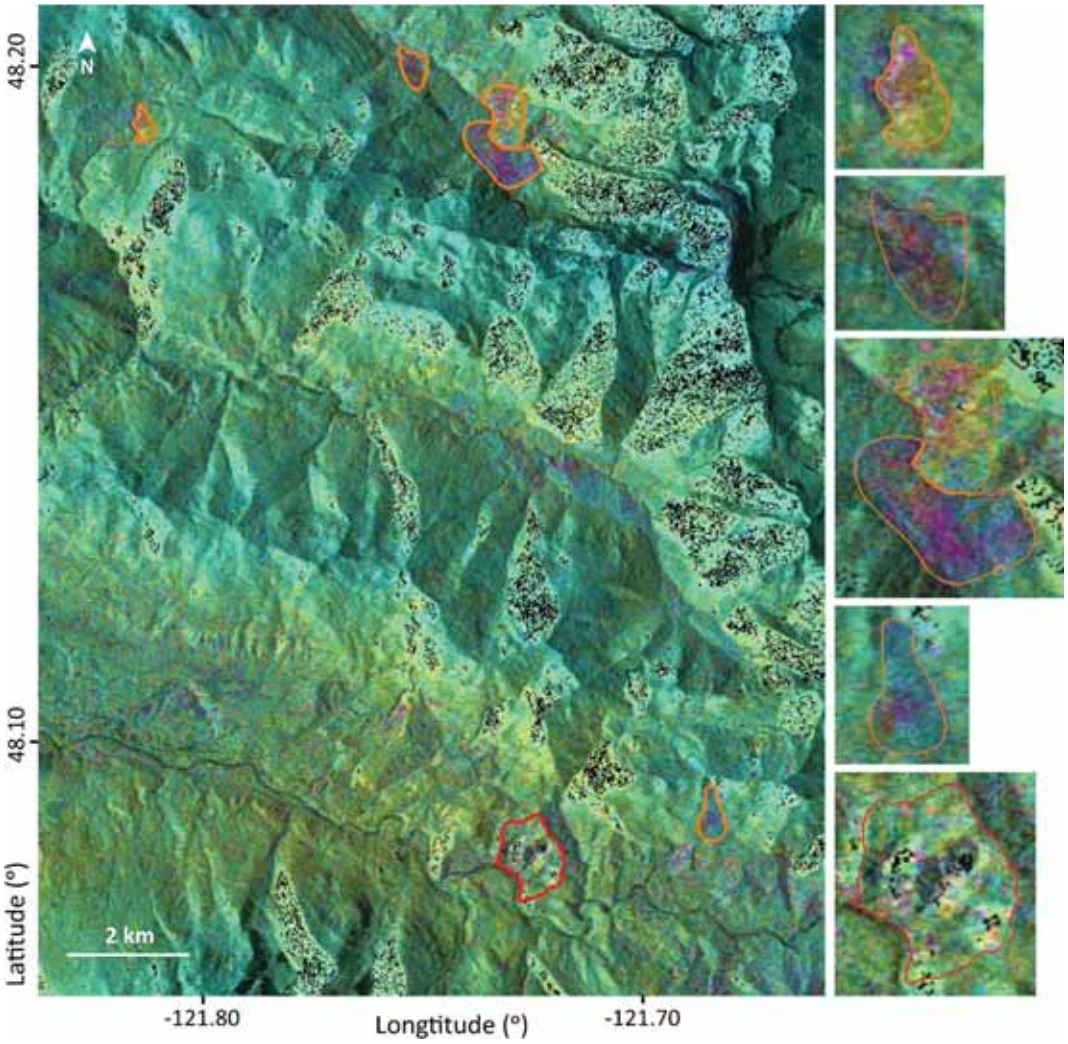

Fig. 6 Detected active landslides nearby Gold Basin from an ALOS-2 interferogram spanning from 2016 to 2017. Small windows on the right show the close-up of each landslide. One fringe represents a line-of-sight range change of 12.1 cm. The Gold Basin landslide complex is outlined in red. Black dots are layover and shadow regions in the right-looking SAR data due to steep topography

by an ALOS-2 interferogram spanning from 2016 to 2017 (Fig. 6), yet deformation signals at the Gold Basin landslide complex were not distinguishable due to poor coherence there. The most likely reason is that the relatively coarse spatial resolution (~ 10 m) and look angle (~35°) of ALOS-2 PALSAR-2 limited its ability to capture highly localized deformation on a steep slope. Indeed, the top 50 m of the middle lobe of the landslide complex is nearly vertical (McCabe 2016; Drury 2001), which would cause shadow or layover effects for the right-side-looking SAR acquisitions (e.g., Hanssen 2001).

SAR intensity changes and pixel offset tracking

As shown in Fig. 7, significant intensity changes of TerraSAR-X SAR images from 2017 to 2019 were detected at the headscarp and western side of the middle valley. The intensity changes varied from − 2 to 2 dB depending on the location. Small intensity changes were observed at the riverbank at the mouth of the middle valley. However, the detected intensity changes do not irrefutably confirm landslide activity, because soil moisture variations or vegetation growth/removal may have also contributed to the changes.

The offset tracking results confirm that localized but significant deformation was present at the middle lobe between 2017 and 2019. The most notable deformation occurred near the headscarp, which shifted by about 10 m. The riverbank near the mouth of the middle valley also had significant erosion of about 7 m. We did not observe any conspicuous signs that would indicate the movement of a large, centralized block, or main body.

Simulations of hypothetical runout scenarios

We simulated 12 scenarios with varied volume-mobility combinations to assess the potential inundation extents of the Gold Basin landslide complex in the event of a failure. Figures 8 and 9 depict the simulated runout scenarios as $m_o - m_{crit} = 0.02$ and $m_o - m_{crit} = -0.02$ respectively. Note that $m_o < m_{crit}$ corresponds to relatively mobile debris flows, while $m_o > m_{crit}$ corresponds to less mobile ones. Comparison of the two groups demonstrates a large disparity in the risk posed to the campground area, based solely on the debris flow mobility given the same initial landslide volume: a more mobile debris flow would cause more damages to the campground by increasing both inundation extent and deposit thickness, provided the same landslide volumes.

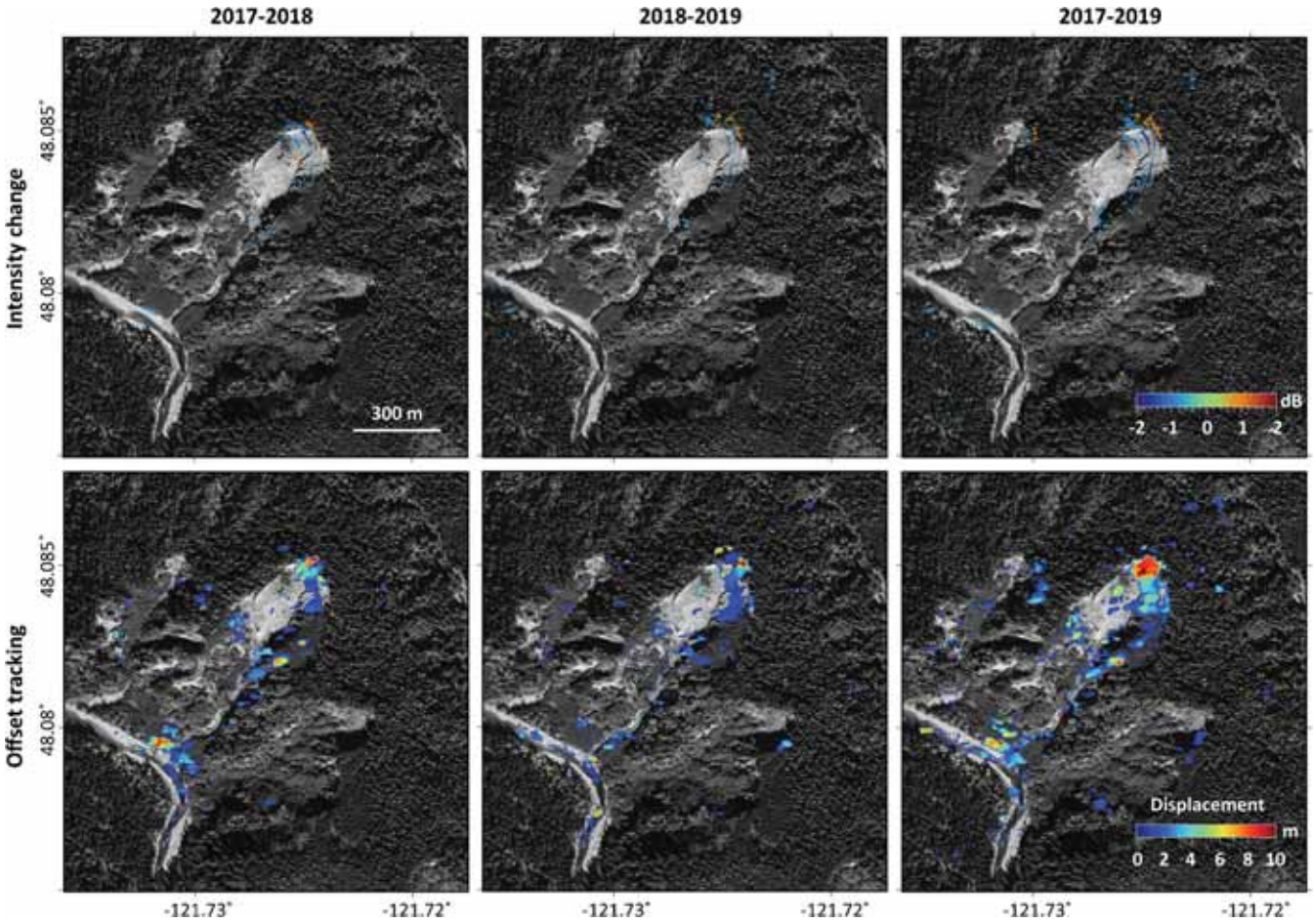

Fig. 7 Intensity changes and tracked displacements of TerraSAR-X images spanning 2017–2018 (left column), 2018–2019 (middle column), and 2017–2019 (right column)

Differencing of 2005 and 2016 LiDAR DEMs indicates an average cumulative landslide volume of 1.03×10^5 m^3 per year (see Section "Landslide volume estimations"), which is approximated by the simulated cases of $V = 1.1 \times 10^5$ m^3. Even the highly mobile simulations with this initial volume pose limited threats to the campground (Fig. 9). Consequently, collapses of the headscarp with volumes less than 10^5 m^3 are unlikely to be of much concern. The simulations agree well with the field observations from US Forest Service that the campground has never experienced any debris flow events since at least 2005.

However, once landslide volumes exceed 10^6 m^3, the simulated debris flows run over the entire campground under both mobility assumptions. As expected, larger volumes tend to increase the runout extent as well as the thickness of deposits on the campground. The estimated maximum landslide volume of 2.0×10^6 m^3 (see Section "Landslide volume estimations") is most closely represented by our simulations with $V = 2.1 \times 10^6$ m^3. As shown in Figs. 8 and 9, our simulations with initial volumes of $V = 2.1 \times 10^6$ m^3 produce debris flows which invariably inundate the entire campground, regardless of their simulated mobility (see supplementary materials for runout animations). The highly mobile debris flow with this initial volume crosses the campground with an 8-m-high flow front. The simulations also suggest that camp sites near the mouth of the middle valley are the most vulnerable to potential runout events.

Discussion

Remotely sensed data such as LiDAR DEMs and SAR provide a means for monitoring landslide motion, at a large scale, in an efficient and cost-effective manner. However, these methods may also present technical and practical challenges for particular difficult cases. For instance, available LiDAR DEMs are typically temporally sparse, while the side-looking angle and spatial resolution of SAR data limit their effectiveness for small landslides in steep or heavily vegetated areas.

Different SAR datasets have varied advantages and disadvantages in terms of landslide mapping. For instance, the L-band ALOS and ALOS-2 SAR sensors have great vegetation penetration but temporally sparse acquisitions. The Sentinel-1A/B datasets provide temporally dense sampling yet coarse resolution in azimuth direction (Xu et al. 2019). The TerraSAR-X images have high spatial resolution but poor vegetation-penetrating capability. While using phase information through InSAR provides the best displacement measurement accuracy, it has limited applicability to cases with severe

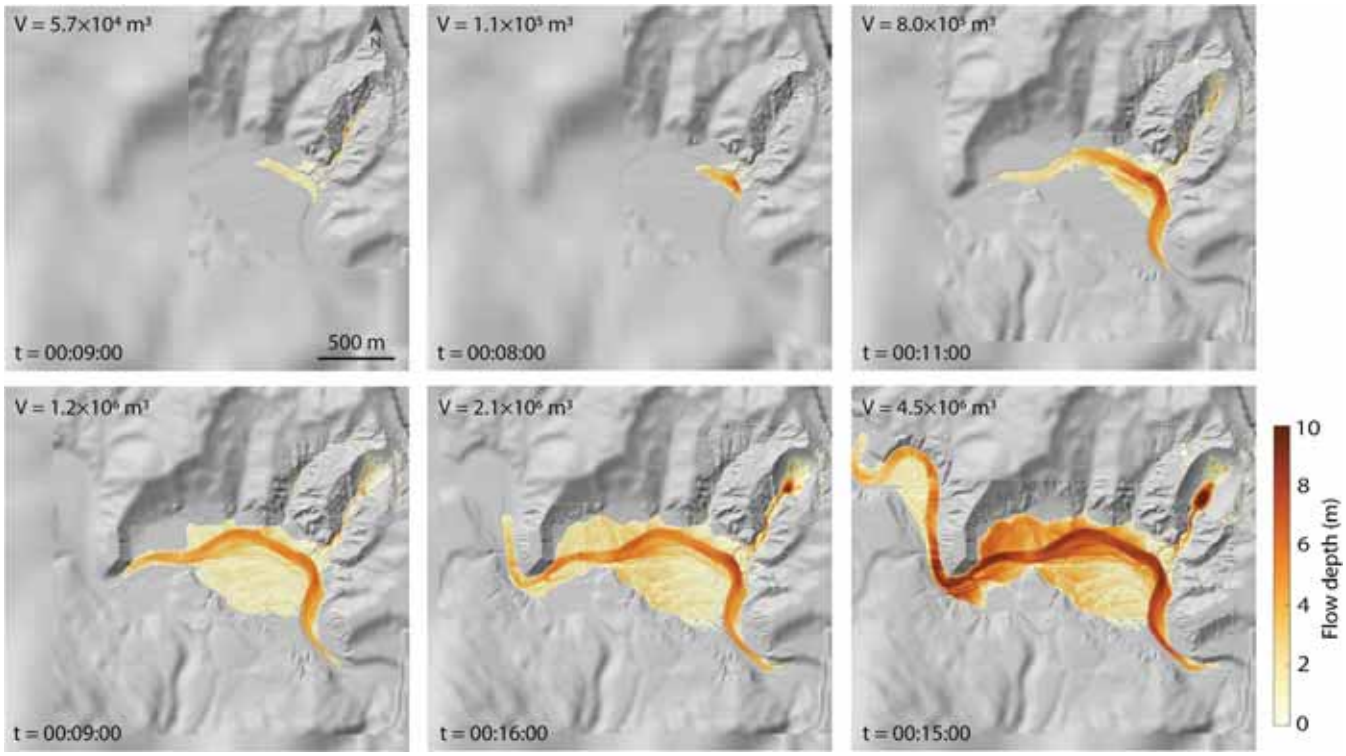

Fig. 8 Maximum campground damages from D-claw simulations with $m_0 - m_{crit} = 0.02$. V denotes volumes ranging from 5.7×10^4 to 4.5×10^6 m^3, and t is the time denoted in hours:minutes:seconds. The highly smooth area near the headscarp of the middle lobe represents the simulated slip surfaces. See supplementary materials for a runout animation of the case $V = 2.1 \times 10^6$ m^3

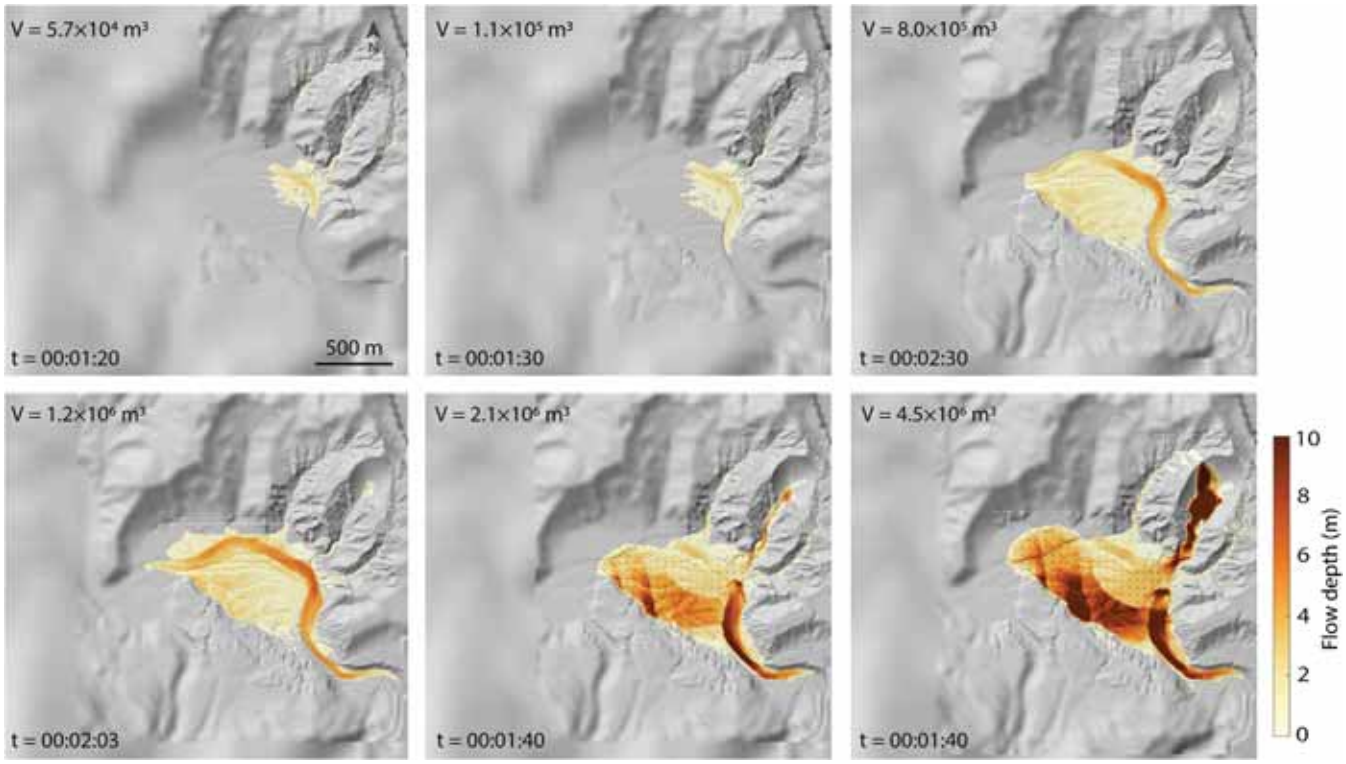

Fig. 9 Maximum campground damages from D-claw simulations with $m_0 - m_{crit} = -0.02$. V denotes volumes ranging from 5.7×10^4 to 4.5×10^6 m^3, and t is the time denoted in hours:minutes:seconds. See supplementary materials for a runout animation of the case $V = 2.1 \times 10^6$ m^3

coherence loss. Such decorrelation might be induced by large displacement, long spatial/temporal baselines, or ground feature changes. In contrast, offset tracking of SAR intensity images is more tolerant to large deformation and temporal/spatial baselines despite of the lower accuracy of 1/20–1/10 pixels (Hanssen 2001). Overall, by combining multiple sources of SAR datasets and employing optimal data processing strategies, we have found that it is possible to maximally harness their combined attributes for landslide monitoring.

LiDAR DEMs are able to provide reliable measurements of landslide activity with small spatial extent, such as headscarp collapses of the Gold Basin landslide complex. However, the high cost of repeated LiDAR acquisitions and the low sensitivity to slow-moving slides comprise substantive disadvantages. Nevertheless, we have shown that the challenges with individual remote sensing technologies can largely be overcome through the simultaneous use of multiple data sources and comprehensive data corroboration.

Modeling of landslide dynamics and inundation given an initial mass failure still presents challenges as well, largely resulting from uncertainties about site-specific subsurface conditions and material properties. However, by considering a range of possibilities, inundation bounds can be approximated to a reasonable degree of certainty, at least for general hazard awareness and effective mitigation strategies.

Conclusions

Applying complementary remote sensing data including LiDAR DEMs and SAR images to surveil stability of the Gold Basin landslide demonstrates that only substantial but localized displacements have occurred at the Gold Basin area between 2005 and 2019. The middle lobe has been the most active, while the eastern-most lobe has been primarily stable during this period. The headscarp of the middle lobe underwent a maximum displacement of approximately 40 m during the past decade, and the western-most lobe has also experienced displacements of about 20 m at the headscarp. Significant erosion was observed at the riverbank near the middle valley after 2017. Average cumulative movement volume of the Gold Basin landslide complex is 1.03×10^5 m^3 per year. Nevertheless, from 2005 to 2019, there is no evidence indicating movement of a large central block or single deep-seated landslide body.

Our practice of interpreting SAR with multiple approaches demonstrates that offset tracking of high-resolution SAR is an effective alternate approach to detect landslide activity if InSAR cannot yield reasonable results due to coherence loss induced by vegetation or steep slope angles.

D-claw runout simulations with multiple landslide volumes and varied runout behaviors show that small collapses of the headscarp with volumes less than 10^5 m^3 will most likely pose a low threat to the campground, while severely hazardous runout might occur if the initial slide is over 10^6 m^3. The estimated maximum volume of the Gold Basin landslide is 2.0×10^6 m^3, indicating a significant hazard to the nearby campground should slope failure induce a mobile landslide. The runout potential of such a landslide would depend on the landslide mobility, which is dependent on material parameters that are difficult to constrain due to uncertainties about the subsurface conditions. Nevertheless, flow simulations provide evidence about the range of possible outcomes and inform hazard mitigation.

In this investigation, we have proven the possibility of using remotely sensed data to measure deformation occurring in a difficult terrain by integrating multiple data sources and comprehensive data processing strategies. Furthermore, we have presented a means of evaluating runout hazards of a landslide by employing the numerical model D-claw. Most importantly, the methods developed for this case study can be easily adapted for other similar landslides globally to assist on landslide hazards prevention and mitigation.

Funding This project was financially supported by NASA Interdisciplinary Research (IDS) in Earth Science Program (80NSSC17K0022), US Forest Service (16-CR-11062761-035), and the Shuler-Foscue Endowment at Southern Methodist University.

References

Angeli MG, Pasuto A, Silvano S (2000) A critical review of landslide monitoring experiences. Eng Geol 55:133–147

Baker R, Garber M (1978) Theoretical analysis of the stability of slopes. Geotechnique 28:395–411

Benda L, Collins B (1992) Slope stability investigation of the Crown Pacific Property in the South Fork of the Stillaguamish River Basin, unpublished report, 37 p

Chen WF (Edition 1) (1975) Limit analysis and soil plasticity. 7:1–638

Colesanti C, Wasowski J (2006) Investigating landslides with space-borne Synthetic Aperture Radar (SAR) interferometry. Eng Geol 88(3-4):173–199

Drury AT (2001) Gold Basin landslide remediation feasibility study, alternatives development and analysis, and preliminary project designs, RM 48, SF Stillaguamish River, Prepared for The Stillaguamish Tribe of Indians, 45p

Fruneau B, Achache J, Delacourt C (1996) Observation and modelling of the Saint-Etienne-de-Tinée landslide using SAR interferometry. Tectonophysics 265(3-4):181–190

George DL, Iverson RM (2014) A depth-averaged debris-flow model that includes the effects of evolving dilatancy. II. Numerical predictions and experimental tests. Proc R Soc A: Math Phys Eng Sci 470(2170):20130820

Hanssen RF (2001) Radar interferometry: data interpretation and error analysis (remote sensing and digital image processing). Springer Netherlands. https://doi.org/10.1007/0-306-47633-9

Hodgson ME, Jensen JR, Schmidt L, Schill S, Davis B (2003) An evaluation of LIDAR-and IFSAR-derived digital elevation models in leaf-on conditions with USGS Level 1 and Level 2 DEMs. Remote Sens Environ 84(2):295–308

Iverson RM, George DL (2014) A depth-averaged debris-flow model that includes the effects of evolving dilatancy. I. Physical basis. Proc R Soc A: Math Phys Eng Sci 470(2170):20130819

Iverson RM, Reid ME, Iverson NR, LaHusen RG, Logan M, Mann JE, Brien DL (2000) Acute sensitivity of landslide rates to initial soil porosity. Science 290:513–516

Iverson RM, Logan M, LaHusen RG, Berti M (2010) The perfect debris flow? Aggregated results from 28 large-scale experiments. JGR Earth Surf 115(F3)

Iverson RM, George DL, Allstadt K, Reid ME, Collins BD, Vallance JW, Schilling SP, Godt JW, Cannon CM, Magirl CS, Baum RL (2015) Landslide mobility and hazards: implications of the 2014 Oso disaster. Earth Planet Sci Lett 412:197–208

Lu Z, Dzurisin D (2014) InSAR imaging of Aleutian volcanoes: monitoring a volcanic arc from space: Springer Praxis Books, Geophysical Sciences, Springer, p 390. https://doi.org/10.1007/978-3-642-00348-6

McCabe C (2016) Using Terrestrial LiDAR to Monitor Erosion within the Gold Basin Landslide Complex, Verlot, WA. Master's thesis, University of Washington. http://hdl.handle.net/1773/36260

Miller DJ (2019) Gold basin and steelhead haven: landslides on the Stillaguamish. Provided by M2 Environmental Services, pp. 1–37

Miller DJ, Miller LR (1999) Hazel/gold basin landslides: geomorphic review draft report. provided by m2 environmental services on behalf of the US army corps of engineers, pp. 1–26

Perkins JP, Reid ME, Schmidt KM (2017) Control of landslide volume and hazard by glacial stratigraphic architecture, northwest Washington State, USA. Geology 45:1139–1142

Plank S, Twele A, Martinis S (2016) Landslide mapping in vegetated areas using change detection based on optical and polarimetric SAR data. Remote Sens 8(4):307

Roering JJ, Stimely LL, Mackey BH, Schmidt DA (2009) Using DInSAR, airborne LiDAR, and archival air photos to quantify landsliding and sediment transport. Geophys Res Lett 36:L19402

Shannon Wilson Engineers (1954) Report on slide on South Fork Stillaguamish River at Gold Basin forest camp, to the State of Washington Departments of Fisheries, 14p

Singleton A, Li Z, Hoey T, Muller JP (2014) Evaluating sub-pixel offset techniques as an alternative to D-InSAR for monitoring episodic landslide movements in vegetated terrain. Remote Sens Environ 147:133–144

Squarzoni C, Delacourt C, Allemand P (2003) Nine years of spatial and temporal evolution of the La Valette landslide observed by SAR interferometry. Eng Geol 68(1-2):53–66

Staisch LM (2018) Bedrock mapping and seismic hazard assessment at gold basin landslide, Washington. US Department of the Interior, US Geological Survey. https://doi.org/10.3133/ofr20181132

Strozzi T, Luckman A, Murray T, Wegmuller U, Werner CL (2002) Glacier motion estimation using SAR offset-tracking procedures. IEEE Trans Geosci Remote Sens 40:2384–2391

Terzis A, Anandarajah A, Moore K, Wang I (2006) Slip surface localization in wireless sensor networks for landslide prediction. In 2006 5th International Conference on Information Processing in Sensor Networks (pp. 109–116). IEEE. https://doi.org/10.1145/1127777.1127797

Wartman J, Montgomery DR, Anderson SA, Keaton JR, Benoît J, dela Chapelle J, Gilbert R (2016) The 22 March 2014 Oso landslide, Washington, USA. Geomorphology 253:275–288

Xu Y, Kim J, George DL, Lu Z (2019) Characterizing seasonally rainfall-driven movement of a translational landslide using SAR imagery and SMAP soil moisture. Remote Sens 11:2347

Electronic supplementary material The online version of this article (https://doi.org/10.1007/s10346-020-01533-0) contains supplementary material, which is available to authorized users.

Y. Xu (✉) · **J. Kim** · **Z. Lu**
Roy M. Huffington Department of Earth Sciences,
Southern Methodist University,
Dallas, TX 75205, USA
Email: yuankunx@smu.edu

D. L. George
U.S. Geological Survey,
Vancouver, WA 98683, USA

M. Riley · **T. Griffin**
U.S. Forest Service, Pacific Northwest Region,
Portland, OR 97204, USA

J. de la Fuente
U.S. Forest Service,
Yreka, CA 96097, USA